HYBRID COMPUTATIONAL SCHEME FOR ANTENNA-HUMAN BODY INTERACTION

K. N. Ramli[1, 2], R. A. Abd-Alhameed[2], C. H. See[2, *], P. S. Excell[3], and J. M. Noras[2]

[1]Faculty of Electrical and Electronics Engineering, Universiti Tun Hussein Onn Malaysia, Parit Raja 86400, Batu Pahat, Johor, Malaysia

[2]Antennas and Applied Electromagnetics Research Group, University of Bradford, Bradford, UK

[3]Glyndwr University, Institute for Arts, Science and Technology, Wrexham, UK

Abstract—A new hybrid method of moments (MoM)/finite-difference time-domain (FDTD), with a sub-gridded finite-difference time-domain (SGFDTD) approach is presented. The method overcomes the drawbacks of homogeneous MoM and FDTD simulations, and so permits accurate analysis of realistic applications. As a demonstration, it is applied to the short-range interaction between an inhomogeneous human body and a small UHF RFID antenna tag, operating at 900 MHz. Near-field and far-field performance for the antenna are assessed for different placements over the body. The cumulative distribution function of the radiation efficiency and the absorbed power are presented and analyzed. The algorithm has a five-fold speed advantage over fine-gridded FDTD.

1. INTRODUCTION

Rigorous determination of electromagnetic fields within arbitrary, anisotropic, and inhomogeneous dielectric bodies is important for researchers exploring the effects of microwaves upon living tissue. Electromagnetic fields are induced inside any biological system, such as the human body, when it is illuminated by an electromagnetic wave, which is also scattered externally. The human body is an irregularly shaped heterogeneous conducting medium whose permittivity and

conductivity vary with the frequency of the incident wave, so the distributions of the internal and scattered electromagnetic fields depend on the body's physiological parameters and geometry, as well as on the polarization and frequency of operation. Due to its mathematical simplicity and ease of implementation, FDTD [1, 2] numerical solutions have been widely adopted to solve complex stratified dielectric objects, such as human bodies [3–5] and biological tissues [6, 7].

The conventional uniform mesh FDTD becomes unfavourable due to excessive computation time and memory when it is applied to electrically small objects which require high spatial resolution. To circumvent this problem, the non-uniform mesh and sub-gridding schemes in FDTD were proposed. However, these methods may produce spurious solutions or suffer from instability [8], so the FDTD method has been used in conjunction with other numerical techniques in order to tackle this limitation. In 1993, Aoyagi et al. [9] used the Yee algorithm in conjunction with the scalar wave equation to reduce the computations needed to model a Vivaldi antenna, while Cangellaris et al. [10] used a hybrid spectral-FDTD method to analyze propagation in anisotropic, inhomogeneous periodic structures. Wang [11] introduced a hybrid ray-FDTD method and used it to investigate scattering from a cavity with a complex termination and wave penetration through inhomogeneous walls. In 1994, Mrozowski [12] introduced a hybrid FDTD-PEE (partial eigenfunction expansion) method to speed up the FDTD method when solving shielded structure problems. In addition, finite element and finite volume methods have recently been combined with FDTD, [13, 14], for accuracy in handling curved geometries and systems with fine features. Hybrid methods operating entirely in the time domain have been reported in the literature [15, 16], but the time-domain MoM is not at the state of maturity and flexibility of the frequency-domain version. Time-domain MoM does have the advantage of generating information over a wide frequency band, and does not need an iterative procedure to couple with FDTD, but it requires very long run-times when treating a junction with more than two wires [17], unlike the frequency domain version in which complex metallic structures may be modeled accurately with lower run-times and with more flexibility in treating different complex geometries.

Reviewing the literature, the hybrid MoM/FDTD method may be said to have been first investigated in 1982, when Taflove and Umashankar [18] used a hybrid FDTD/MoM approach to investigate electromagnetic (EM) coupling problems and aperture penetration into complex geometries and loaded cavities. In 1987, the same authors used an equivalent surface fully enclosing equivalent wire bundles

(concept of equivalent radius) to replace them with a single wire in the FDTD model [19]. Later, the concepts of [18, 19] were deployed in the computer software GEMACS [20] which was developed using method of moments/uniform geometrical theory of diffraction/finite-difference frequency-domain (MoM/UTD/FDFD) hybrids to allow users to model problems with more than one region.

In 2000, Mangoud proposed a hybrid combination of frequency domain MoM and FDTD [21], thus overcoming the drawbacks of homogeneous FDTD and MoM to solve a wide variety of electromagnetic interaction scattering problems. In 2004, a new hybrid method brought together the FDTD, finite-element time-domain (FETD) and method of moments time-domain (MoMTD) methods to analyze problems of thin-wire antennas radiating in the vicinity of arbitrarily-shaped inhomogeneous bodies [22]. From [23], stair case errors [24] from FDTD can be mitigated by using a finite element method (FEM), but this method requires high computational resources. The method in [21] was extended to include the analysis of wide band [25] and dual-band [26] antenna responses using an impedance interpolation method [26] to minimize the computation time on the MoM side.

More recently, the works [21, 25, 26] have been extended by embedding sub-gridding inside an inhomogeneous human body model when the source excitation is a short-range radio frequency identification (RFID) antenna at 900 MHz in the UHF band [27]. The use of sub-gridding in the hybrid MoM-FDTD method ensures that transitions are as reflection-less as possible in order to provide specific animated display movements of the electric and magnetic fields in both the sub-gridded region and main grids. However, curved objects and small geometric features cannot be accurately modelled due to inherent staircase errors caused by the Cartesian grid. To circumvent this weakness, a variable time and space increment has been employed which provides for sub-gridding and consequently minimizes numerical dispersion. The main grid is divided into sub-grids, and the boundary fields are coupled using temporal and spatial interpolations. Thus, the MoM-FDTD-SGFDTD hybridization method is well-suited to electromagnetic radiation and scattering problems as it overcomes the drawbacks of homogeneous MoM and FDTD simulations, this being appropriate for realistic electromagnetic analysis. In this paper, a new 3D hybrid MoM-FDTD-SGFDTD is developed and used to study the state of the art in body-antenna interaction.
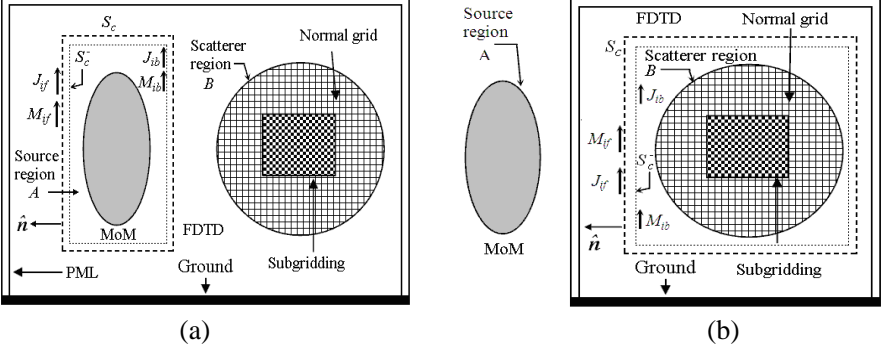
Figure 1. Hybrid MoM-FDTD-SGFDTD configuration for single source and scatterer geometries. (a) Near-field. (b) Far-field.

2. HYBRID MOM-FDTD-SGFDTD THEORETICAL FORMULATION

Consider the electromagnetic hybrid geometry illustrated in Figure 1. The figure shows two regions, with the source in region A, and the scatterer in region B. The source region is bounded by a closed Huygens surface S_c. The method starts by computing the fields due to the real currents of the source region on the surface S_c, excluding region B. These fields are computed by applying Galerkin's method with a set of variable polynomial basis functions [21, 25].

The equivalent surface currents on the surface S_c represent the outward travelling wave-fields from the source to the scatterer, due to the fields of the source. These may be expressed as:

$$J_{if} = \hat{n} \times H_{if} \tag{1}$$
$$M_{if} = E_{if} \times \hat{n} \tag{2}$$

Here $\hat{n}$ is the outwardly directed unit vector normal to the surface from the source region. H_{if} and E_{if} are equivalent to the forward-scattered magnetic and electric fields respectively from the source region on the equivalent surface S_c, and J_{if} and M_{if} are the corresponding electric and magnetic source currents respectively on this surface. These currents are then treated as sources in the FDTD computational province, propagating fields to the scatterer by using the E and H curl equations given by the expression:

$$\nabla \times E = -\frac{\partial B}{\partial t} - M_{if} \tag{3}$$

$$\nabla \times H = -\frac{\partial D}{\partial t} + J_{if} \tag{4}$$

The back-scattered fields were computed by FDTD at S_c^- (the closed surface interior to the surface S_c and bounding the region A). This surface is closed in the scattered field region, so that the calculated surface currents are due to the scattered fields only. The equivalent surface currents due to these fields, representing an additional source to the MoM domain (region A), are given by:

$$J_{ib} = H_{ib} \times \hat{n} \qquad (5)$$

$$M_{ib} = \hat{n} \times E_{ib} \qquad (6)$$

where H_{ib} and E_{ib} are the back-scattered fields computed at S_c^-. Note that $\hat{n}$ is as above, directed outwards from the source region. J_{ib} and M_{ib} are the electric and magnetic equivalent surface currents at S_c^-. Now, the voltage back-scattered in the source region (the excitation for the MoM) can be evaluated using either of the following equations, defined by the reciprocity theorem in the same way as in [21, 25]:

$$V_b = \iint\limits_{S_a} dS_a (J_{ms} \cdot E_{ib}) \qquad (7)$$

$$V_b = \left\langle J_{ib} \cdot E_{ms} - M_{ib} \cdot H_{ms}, dS_c^- \right\rangle \qquad (8)$$

$$V_b = \iint\limits_{S_c^-} dS_c^- \left(J_{ib} \cdot E_{ms} - M_{ib} \cdot H_{ms} \right) \qquad (9)$$

where:

$$E_{ib} = -j\omega A(r) - \nabla V(r) - \frac{1}{\varepsilon} \nabla \times F(r) \qquad (10)$$

$$A(r) = \mu \iint\limits_{S_c^-} dS_c^- \left\{ J_{ib} G\left(r, r'\right) \right\} \qquad (11)$$

$$V(r) = -\frac{j}{\omega\varepsilon} \iint\limits_{S_c^-} dS_c^- \left\{ \nabla'_s \cdot J_{ib} G\left(r, r'\right) \right\} \qquad (12)$$

$$F(r) = \varepsilon \iint\limits_{S_c^-} dS_c^- \left\{ M_{ib} G\left(r, r'\right) \right\} \qquad (13)$$

$G(r, r')$ is the free space Green function, given by the expression:

$$G(r, r') = \frac{e^{-jk|r-r'|}}{|r - r'|} \qquad (14)$$

The vectors r and r' apply to the source and observation points respectively, and S_a is the conducting surface area of the structure

within region A. J_{ms} is the electric test-function used on the wire. E_{ms} and H_{ms} are the electric and magnetic fields respectively for the test-function J_{ms}. Equation (7) explicitly requires a double integral to evaluate E_{ib} and integrate over the surface of the antenna, with the condition that the FDTD discretisation be very small compared to the operating wavelength. It can be simplified by ignoring the surface integral and evaluating the voltage back-scattered corresponding to the centre of the cell surface, by a summation over grid cell surfaces, to get the following equation for the hybrid case:

$$V_b = \sum_{k=1}^{n_{S_c^-}} \left(J_{ib_k} \cdot E_{ms}(r_k, r') - M_{ib_k} \cdot H_{ms}\left(r_k, r'\right) \right) a_k \qquad (15)$$

where r_k is the position vector of the centre of the cell surface and a_k is the surface area of the cell surface. Therefore J_{ib_k} and M_{ib_k} are the equivalent surface currents at the centre of the surface cell n. Since the excitation voltages are known, the MoM can be executed to compute the new currents and the procedure can be repeated until the steady state solution is achieved.

3. VALIDATION OF THE METHOD

In this section, two examples will be given in order to establish a better evaluation of the numerical efficiency and accuracy of the proposed algorithm.
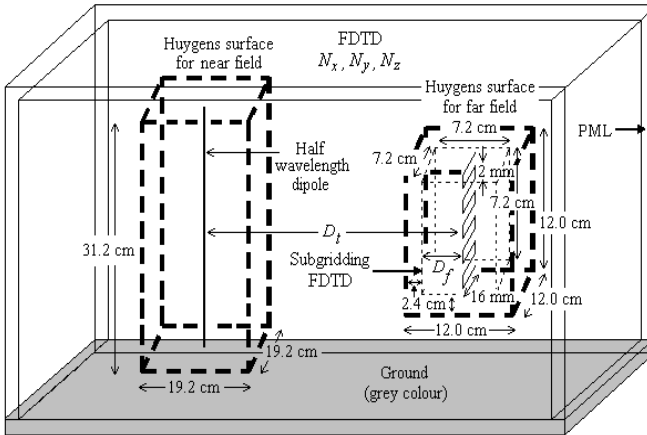

Figure 2. A basic geometry of FDTD-SGFDTD for near-field and far-field validation.

3.1. RFID Reader and Tag Antennas Model

A 900 MHz centre-fed half-wavelength dipole of 0.0025λ radius was defined as a transmitter source, for example presenting the RFID reader, whereas the RFID tag was considered as a small half-wavelength meander antenna [28], as shown in Figure 2. The tag was designed in a zig-zag pattern with 17 turns in which sub-gridding cells of $6 \times 6 \times 6$ volumetric were imposed. The dotted bold line on the left and right portray the Huygens surface for near and far field respectively. The spatial resolution of the computational domain was terminated by six faces of perfectly matched layer (PML) in which one of them describes the ground plane (represented by grey colouring in the figure). Two different distances between the source and the tag were studied and discussed, for the far-field and near-field cases, with separate simulations for each. It should be noted that the centres of the source and the sensor lie on the y axis and they are separated by the distance D_t. For both simulations, a thin wire subroutine code inside the sub-gridded FDTD was used to include the effects of the wire radius of the meander antenna inside the new FDTD sub-grid. For simplicity in this example the medium surrounding the source and the scatterer was modelled as free space; however, in general the scatterer can be placed on dielectric objects in which part of its volume can be sub-gridded.

A sinusoidal excitation voltage was applied at the centre of the antenna source. The antenna wires were assumed to be perfectly conducting. The near-field method as shown in Figure 1(a) is equivalent to the far-field configuration for short distances, such as
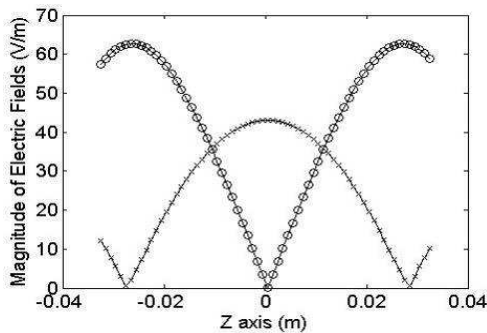

Figure 3. Magnitude of E_y and E_z electric field components along z axis at $y = 7.2$ cm. Near-field E_y ('∘ ∘ ∘'), E_z ('× × ×'), Far-field E_y and E_z ('—').

$D_t = 16.8$ cm. In contrast, the far-field technique as illustrated in Figure 1(b) is analogous to the near-field configuration for much higher distances, such as $D_t = 33.6$ cm. The magnitude of E_y electric field components along the z axis at $y = 7.2$ cm were compared for near-field and far-field simulations, with good agreement as shown in Figure 3. The E_z components were also assessed and found to be identical to each other (see Figure 3). The field distribution over an x-z plane 7.2 cm distant from the sensor for the near-field and far-field technique is shown in Figures 4(a) and (b) respectively. The plane size considered here was 20 cm $\times$16 cm for the x and z axes respectively. When the far-field and near-field techniques were checked for comparison of one antenna geometry i.e., with D_t was set at 16.8 cm for both techniques, the fields were found identical to each other. Both methods show good stability and the results were convergent within four iterations. However, the total field components were found to vary between $\pm 2\%$ when compared to results computed using Numerical Electromagnetic Code (NEC) software.
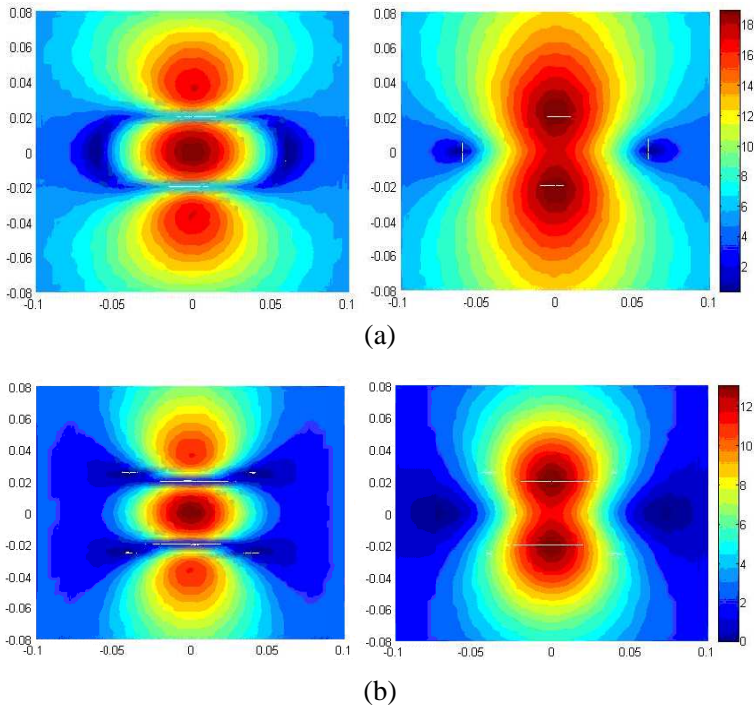

(a)

(b)

Figure 4. A basic distribution of the E_z and E_{total} field components in dB at 7.2 cm away from the sensor, (a) using near field method and (b) using far field method. (left: E_z, right: E_{total}).
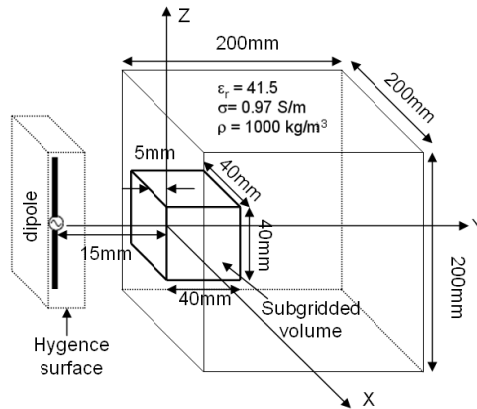
Figure 5. Basic geometry model of COST244.

3.2. COST 244 Model

To further validate the accuracy of the proposed method, where Figure 5 depicts the calculation model used, and to compare the result with existing published results [3, 29], a COST244 model [3, 29] was adopted as a human phantom. This model represents a homogeneous cubical human head of size $200 \times 200 \times 200 \, \text{mm}^3$, with relative permittivity $\varepsilon_r = 41.5$, conductivity $\sigma = 0.95 \, \text{S/m}$ and volume density $\rho = 1000 \, \text{kg/m}^3$.

A 160 mm long half-wavelength dipole, operating at 900 MHz, was used as a radiation source, with a continuous wave with an input power of 250 mW exciting the dipole. The distance between the antenna and the human head was 15 mm and the origin of coordinates was set at the centre of the surface of the human head model, on the same horizontal level as the antenna feeding point.

The FDTD cell size and time step in the analysis area were 2.5 mm and 3.3 ps respectively. The problem space, cell sizes and number of PML layers were $(127 \times 127 \times 127 \text{ cells})$, 2.5 mm and 6, respectively. The size of the equivalent Huygens surface is $6 \times 6 \times 68$ cells, equivalent to 15 mm $\times 15$ mm $\times 170$ mm. The sub-gridded volume is $16 \times 16 \times 16$ cells, equivalent to 40 mm $\times$ 40 mm $\times 40$ mm. It should be noted that this sub-gridded volume is placed between two dielectric media, i.e., free space $(40 \times 5 \times 40 \, \text{mm}^3)$ and the human head $(40 \times 35 \times 40 \, \text{mm}^3)$ in order to evaluate the effectiveness of the proposed method when applied to inhomogeneous tissues. Two and four sub-gridding factors were used for each cell of the main FDTD. The dielectric properties for the sub-gridded cells located on the boundary were averaged and
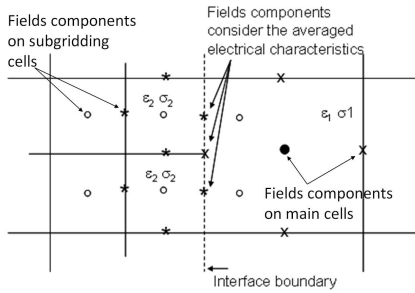
Figure 6. Distribution of field components on the interface boundary model of two different mediums of the proposed sub-gridding model.
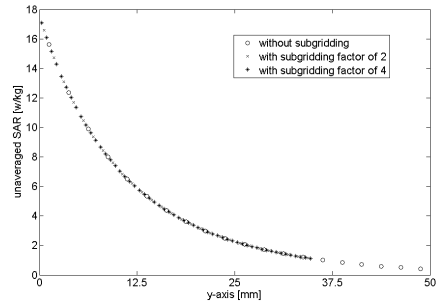
Figure 7. The variations of the unaveraged SAR along y-axis of the model shown in Figure 2 [3, 29].

assigned on each field component, as shown in Figure 6. The variations of the unaveraged specific absorption rate (SAR) along the y-axis with and without sub-gridding are shown in the Figure 7. These unaveraged SAR values without sub-gridding, with sub-gridding factor of 2 and with sub-gridding factor of 4 were observed at every 1.25 mm, 0.625 mm and 0.3125 mm points respectively in the ascending order along the y-axis. The outcomes were promising for the case of without subgridding and both with sub-gridding factors applied in this example due to the convergence of the results into one line. The averaged SAR of 6.8 W/kg was computed by numerical simulation (in this case, it was averaged) over 10 gm of human tissue. The value of 6.8 W/kg (averaged over 10 gm of tissue) when compared with [3, 29] which is about 6.76 W/kg, were very close.

In order to prove the proposed technique is computationally viable, the situation shown in Figure 5 was also modeled using FDTD with coarse and fine grids, and using FDTD/MoM methods. The required computational times for each method are compared in Table 1. In the coarse grid FDTD model, a 2.5 mm cell size was used while in the fine grid FDTD model, 1.25 mm and 0.625 mm cell sizes were adopted. It should be noted that all simulations were performed on an Intel Core-i7-2000 desktop with 3.4 GHz CPU and 16 GB of RAM. As can be noticed, the proposed method exhibits reasonable computational time in comparison with the standard coarse-gridded FDTD and MoM/FDTD. However, when compared with fine-gridded FDTD, the proposed algorithm requires less computational effort, yielding roughly a five-fold speed improvement.

Table 1. Simulation time for different numerical techniques.

| Method	Problem space size	Cell size (mm)	Time steps (ps)	No of steps/ number of cycles	Simulation Time (hours)
FDTD	$127 \times 127 \times 127$	2.5	3.3	8417 (25 cycles)	1.5
FDTD	$254 \times 254 \times 254$	1.2	1.041	26683 (25 cycles)	4.5
FDTD	$508 \times 508 \times 508$	0.625	0.7	39682 (25 cycles)	17
MOM/FDTD	$127 \times 127 \times 127$	2.5	3.3	8417 (25 cycles)	3.8
MOM/FDTD/SG (subgridding factor 2)	$127 \times 127 \times 127$ SG $16 \times 16 \times 16$	2.5	3.3	8417 (25 cycles)	4.1
MOM/FDTD/SG (subgridding factor 4)	$127 \times 127 \times 127$ SG $16 \times 16 \times 16$	2.5	3.3	8417 (25 cycles)	4.3
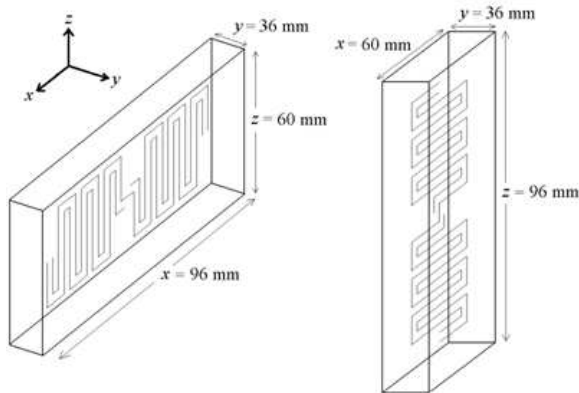
Figure 8. RFID antenna with equivalent Huygens box. (a) Horizontal polarization. (b) Vertical polarization.

4. RESULTS AND DISCUSSION

A Huygens surface around the proposed antenna is first introduced as illustrated in Figure 8 with volume of $16 \times 4 \times 10$ and $10 \times 4 \times 16$

FDTD cells for horizontal and vertical polarization respectively. The surface basically acts as a virtual box enclosing the radiating element such that the fields are enclosed within this region.

The equivalent electric and magnetic sources on the Huygens surface are produced at each time step from the electric and magnetic fields created by the antenna in free space using NEC code [30]. This field data is used as an input source for the FDTD code. The overall FDTD spatial volume is $118 \times 77 \times 327$ points. The equivalence principle is carried out in 3-D by applying the hybrid electromagnetic method described in [28] with cell size $dx = dy = dz = 6.0\,\text{mm}$ and $dx = dy = dz = 3.0\,\text{mm}$ for the coarse and fine FDTD lattices respectively. The time step is set at 7.0 ps. A 6 cell perfectly matched layer (PML) is used to terminate the FDTD space, and the distance between the antenna Huygens surface box and the human body is
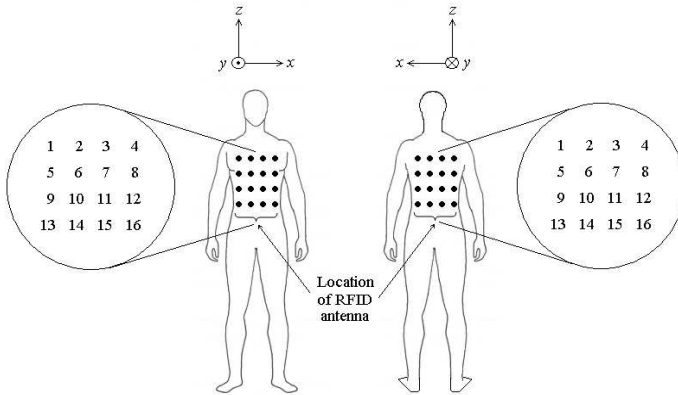

Figure 9. Location of the antennas, represented by black dots, in proximity to the human body.
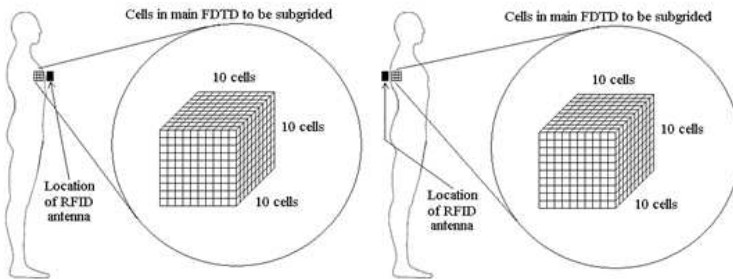

Figure 10. Sub-grid cells of $10 \times 10 \times 10$ FDTD cells are taken inside the human body. (a) Front location. (b) Back location. (sub-gridded).

12.0 mm (or 2 cells). The human body model employed in this work was developed by Mason et al. in 2000 [31]. The near-field and far-field radiation of the antenna at 900 MHz for different locations has been analyzed in order to investigate the performance of the antenna in proximity to the human body. The number in Figure 9 indicates the location of the RFID antenna. A total of 32 locations were investigated; 16 on the back, and 16 on the front. Each placement was investigated with horizontal and vertical polarizations, in order to obtain the clearest possible results with a restricted number of samples.

Figure 10 shows the location of the antenna in front and at the back of human body respectively, in which sub-grid cells of $10 \times 10 \times 10$
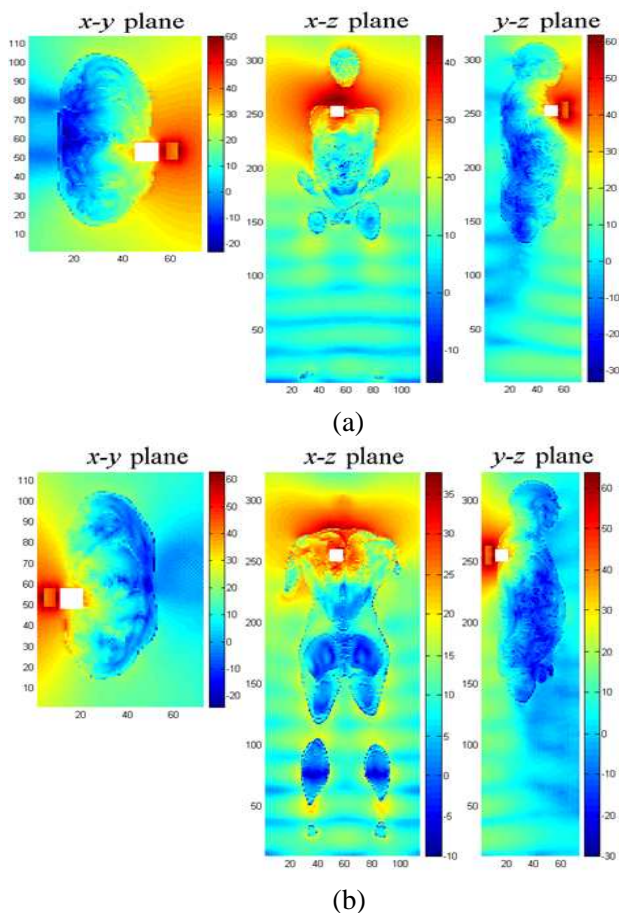

(a)

(b)

Figure 11. Electric field distribution (dB scale) for vertical polarized antenna placed at: (a) front of the body, (b) back of the body.

FDTD cells were taken inside the human body for near-field analysis. The near-field and far-field of the antenna are calculated and analyzed at various locations in order to build up a realistic picture of the antenna performance while in close proximity with the human body. Figure 11 shows the electric field distributions using an equivalent dB scale in the immediate neighbourhood and the interior of the body model, for the vertical polarization state, in x-y, x-z and y-z planes. Figure 12 shows the electric field distribution inside the sub-gridded region for x-y, x-z and y-z planes (represented in the equivalent dB scale). Additional simulations were performed using the same antenna placements for horizontally polarized antenna, and these were found to be comparable with the vertical state. The electric field distributions obtained in the neighbourhood of the human body model were almost the same regardless of whether the antenna tag was horizontally or vertically polarized. It is interesting to note that a similar observation was also produced within the sub-gridded region. The electric fields were very strong when the antenna was located close to the body, as represented by the red colouring in the plots.

Figure 13 illustrates the far-field radiation pattern for the antenna (in horizontal polarization state) at the front and back of the human body model. It should be noted that the underlying computation was normalized to 1 W input power. The variation in the far-field patterns implies that the field distributions are more concentrated in the direction facing the normal antenna axis, and away from the body. The field magnitude is reduced by between 10 dB to 20 dB,
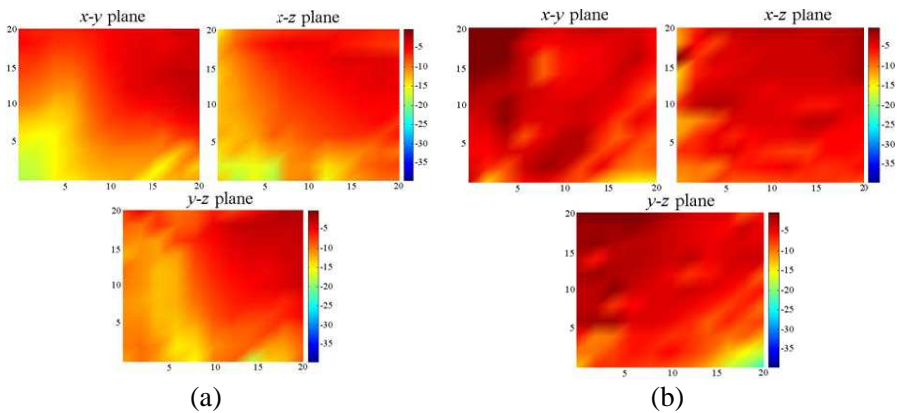

Figure 12. Electric field distribution (dB scale) inside sub-grid region for vertically polarized antenna placed at: (a) front of the body. (b) back of the body.
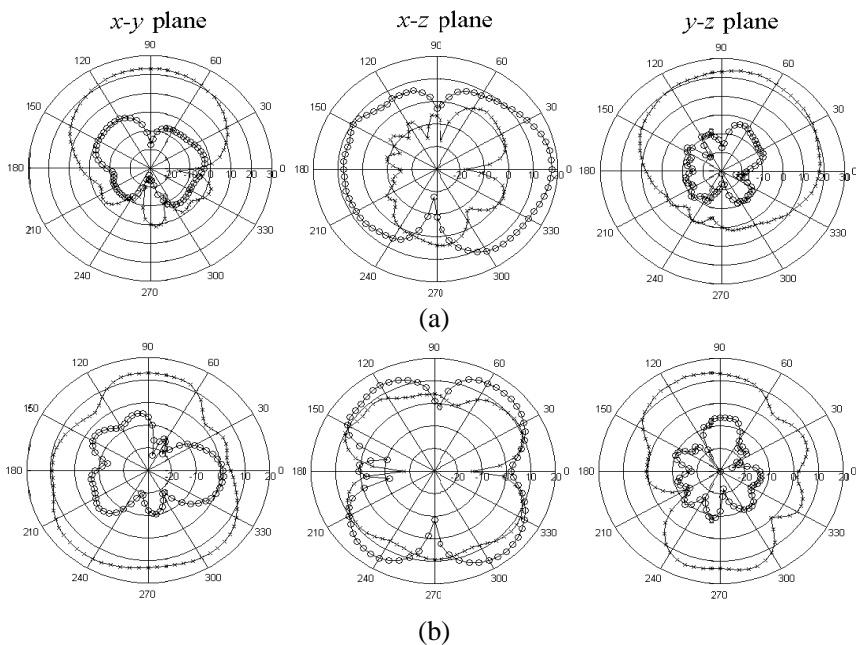
Figure 13. Far-field pattern for horizontally polarized antenna placed at: (a) front of the body, (b) back of the body; 'o-o-o': E_θ, '×-×-×': E_ϕ.

which appears to be due to the tailing effect of the body. Once more, the field distributions for vertical polarization were quite similar to the horizontal case, and hence are not reproduced here.

It can be concluded from Figure 14 that the cumulative distribution function (CDF) has similar curves for horizontal and vertical polarization in these locations. Moreover, it is apparent that the standard deviation of the radiation efficiency when the mobile is located in the front is less compared to the back. The antenna achieves better radiation efficiency of 43% mean percentage value for both horizontal and vertical polarization comparing front and back location. This follows from a loss in the tissue at the front, and a greater degree of absorbed power at the back of the human body, as can be seen from the plots. Taking the previous simulation results into account, we may conclude that altering the position of the antenna on the front will not result in a large dispersion in the radiation efficiency of the antenna.
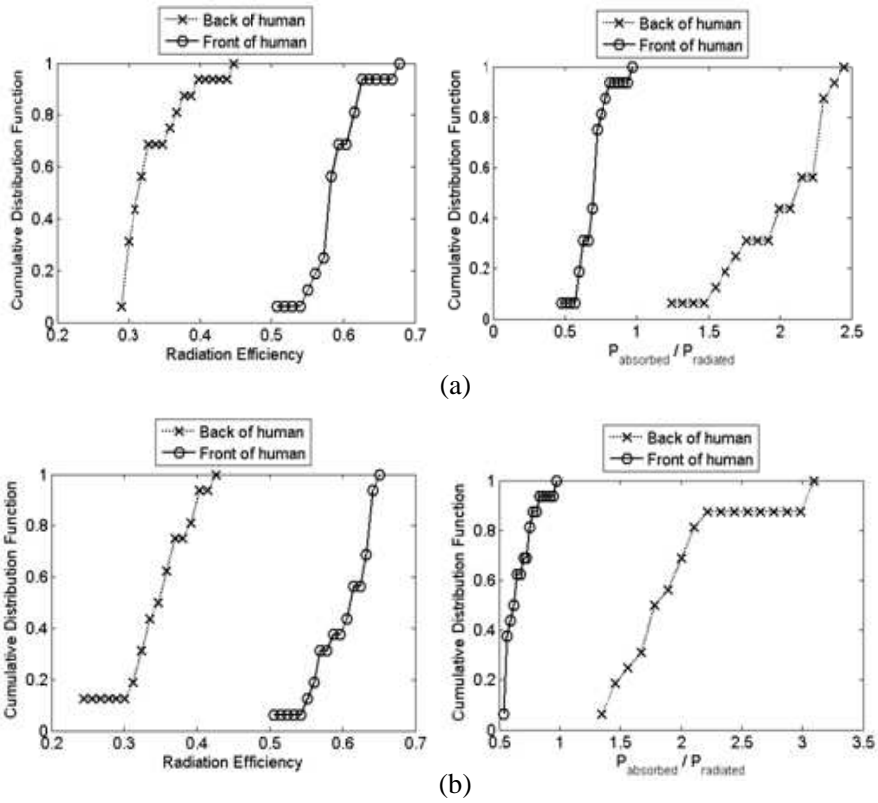
Figure 14. Cumulative distribution function of radiation efficiency and the ratio of $P_{absorbed}/P_{radiated}$ for: (a) horizontal polarized antenna, (b) vertical polarized antenna.

5. CONCLUSION

A hybrid MoM-FDTD-SGFDTD approach has been presented and adopted for modeling the interaction of the human body with a short-range RFID antenna. In order to ensure that optimal quality of results was achieved using a limited sample size of 32 points, each point was investigated using two both horizontal and vertical polarizations. The MoM technique was used to produce the electric and magnetic fields created by the antenna in free space, and the equivalent electric and magnetic sources on the Huygens surface were produced at each time step. The FDTD technique was then applied for the whole structure of the problem combined with sub-gridding at the object of interest, namely inside the human body near the excitation source.

The human body model was designed to be inhomogeneous at close proximity to the antenna. The near-field and far-field distributions were incorporated into the study to heighten the understanding of the impact on human tissue both facing the antenna, and not directly facing the antenna. The cumulative distribution function of the radiation efficiency and the ratio of absorbed to radiated power of the antenna at these locations were also computed. The results support the conclusion that there was a clear improvement in the front of the human body model compared to the back position. The combination of hybrid MoM-FDTD-SGFDTD method approach with an arbitrary inhomogeneous human body model encourages the development of this new EM field interaction modeling approach. This study robustly supports the computing of the total power dissipated and the SAR distribution inside human tissue.

REFERENCES

1. Yee, K. S., "Numerical solution of initial boundary value problems involving Maxwell's equations in isotropic media," *IEEE Trans. on Antennas and Propagation*, Vol. 14, No. 8, 302–307, May 1966.

2. Taflove, A., "Application of the finite-difference time-domain method to sinusoidal steady-state electromagnetic penetration problems," *IEEE Trans. Electromagnetic Compatibility*, Vol. 22, No. 3, 191–202, Aug. 1980.

3. Kawai, H. and K. Ito, "Simple evaluation method of estimating local average SAR," *IEEE Trans. Microw. Theory Tech.*, Vol. 52, No. 8, 2021–2029, Aug. 2004.

4. Fujii, K., M. Takahashi, and K. Ito, "Electric field distributions of wearable devices using the human body as a transmission channel," *IEEE Trans. on Antennas and Propagation*, Vol. 55, No. 7, 2080–2087, Jul. 2007.

5. Jung, J.-H., S.-W. Kim, Y.-S. Kim, and S.-Y. Kim, "Electromagnetic propagation from the intestine-ingested source in the human body model," *IEEE Trans. on Antennas and Propagation*, Vol. 58, No. 5, 1683–1688, May 2010.

6. Emili, G., A. Schiavoni, F. L. Roselli, and R. Sorrentino, "Computation of electromagnetic field inside a tissue at mobile communications frequencies," *IEEE Trans. Microw. Theory Tech.*, Vol. 51, No. 1, 178–186, Jan. 2003.

7. See, C. H., R. A. Abd-Alhameed, and P. S. Excell, "Computation of electromagnetic fields in assemblages of biological cells using

a modified finite-difference time-domain scheme," *IEEE Trans. Microw. Theory Tech.*, Vol. 55, No. 9, 1986–1994, Sep. 2007.

8. Monk, P. and E. Suli, "Error estimates for Yee's method on nonuniform grids," *IEEE Trans. Magn.*, Vol. 30, No. 5, 3200–3203, Sep. 1994.

9. Aoyagi, P. H., J. F. Lee, and R. Mittra, "A hybrid Yee algorithm/scalar-wave equation approach," *IEEE Trans. Microw. Theory Tech.*, Vol. 41, 1593–1600, 1993.

10. Cangellaris, A. C., M. Gribbons, and G. Sohos, "A hybrid spectral/FDTD method for the electromagnetic analysis of guided waves in periodic structures," *IEEE Transactions Guided Wave letters*, Vol. 3, 375–377, 1993.

11. Wang, Y., S. K. Chaudhuri, and S. Safavi-Naeini, "An FDTD/ray-tracing analysis method for wave penetration through inhomogeneous walls," *IEEE Transactions on Antennas and Propagations*, Vol. 50, 1598–1604, 2002.

12. Mrozowski, M., "A hybrid PEE-FDTD algorithm for accelerated time domain analysis of electromagnetic waves in shielded structures," *IEEE Microwave Guided Wave Letters*, Vol. 4, 323–325, 1994.

13. Monorchio, A. and R. Mittra, "Time-domain (FE/FDTD) technique for solving complex electromagnetic problems," *IEEE Microwave Guided Wave Letters*, Vol. 8, 93–95, 1998.

14. Fierriers, X., J.-P. Parmantier, S. Bertuol, and A. R. Ruddle, "Application of hybrid finite difference/finite volume method to solve an automotive EMC problem," *IEEE Transactions on Electromagnetic Compatibility*, Vol. 4, 624–634, 2004.

15. Cerri, G., P. Russo, A. Schiavoni, G. Tribellini, and P. Bielli, "MoM-FDTD hybrid technique for analysing scattering problems," *Electronic Letters*, Vol. 34, 433–440, 1998.

16. Bretones, A. R., A. Monorchio, G. Manara, R. G. Martin, and R. Mittra, "Hybrid technique combining finite element, finite difference and integral equation methods in the time domain," *Electronic Letters*, Vol. 36, 506–508, 2000.

17. Tinniswood, A. D., "Time domain integral equations," Ph.D. Dissertation, University of York, 1996.

18. Taflove, A. and K. R. Umashankar, "A hybrid moment method/finite difference time-domain approach to electromagnetic coupling and aperture penetration into complex geometries," *IEEE Trans. on Antennas and Propagation*, Vol. 30, 617–627, 1982.

19. Umashankar, K. R., A. Taflove, and B. Beker, "Calculation and experimental validation of induced currents on coupled wires in an arbitrary shape cavity," *IEEE Trans. on Antennas and Propagation*, Vol. 35, 1248–1257, 1987.

20. Coffey, E. L. and D. L. Kadlec, "General electromagnetic model for the analysis of complex systems (GEMACS) version 5.0," *Advanced Electromagnetic Corporation for USAF Rome Air Development Center (USA), Report No. RADC-TR-90-360*, Vol. I–III, 1990.

21. Mangoud, M. A., R. A. Abd-Alhameed, and P. S. Excell, "Simulation of human interaction with mobile telephones using Hybrid techniques over coupled domains," *IEEE Trans. Microw. Theory Tech.*, Vol. 48, 2014–2021, 2000.

22. Monorchio, A., A. R. Bretones, R. Mittra, G. Manara, and R. G. Martin, "A hybrid time-domain technique that combines the finite element, finite difference and method of moment techniques to solve complex electromagnetic problems," *IEEE Trans. on Antennas and Propagation*, Vol. 52, 2666–2674, 2004.

23. Alias, R., R. A. Abd-Alhameed, P. S. Excell, and Q. Gassim, "A modified equivalent conducting surface boundary using the hybrid FEM-FDTD technique," *8th IEEE International Multi-topic Conference (INMIC2004)*, NUCES FAST, Lahore, Pakistan, 698–702, Dec. 24–26, 2004.

24. Akyurtlu, A., D. H. Werner, V. Veremey, D. J. Steich, and K. Avdin, "Staircasing errors in FDTD at an air-dielectric interface," *IEEE Microwave Guided Wave Letters*, Vol. 9, 444–446, 1999.

25. Abd-Alhameed, R. A., P. S. Excell, and M. A. Mangoud, "Broadband antenna response using hybrid technique combining frequency domain MoM and FDTD," *Eleventh International Conference on Antennas and Propagation*, Vol. 20, 857–860, 2001.

26. Alhaddad, A. G., R. A. Abd-Alhameed, D. Zhou, C. H. See, I. T. E. Elfergani, and P. S. Excell, "Low profile dual-band balanced handset antenna with dual-arm structure for WLAN application," *IET Microwaves, Antennas & Propagation*, Vol. 5, 1045–1053, Jun. 2011.

27. Ramli, K. N., R. A. Abd-Alhameed, Y. A. S. Dama, M. S. A. Alkhambashi, M. B. Child, and P. S. Excell, "Interaction of EM fields to the human body using MoM-FDTD-SGFDTD hybrid computational method," *EMC Europe*, 26–30, York, UK, Sep. 1–4, 2011.

28. Abd-Alhameed, R. A., P. S. Excell, C. H. See, D. Zhou,

and K. N. Ramli, "Accurate field distribution models for RFID applications using hybrid computational electromagnetics techniques," *PIERS Proceedings*, 436–442, Cambridge, USA, Jul. 2–6, 2008.

29. Kajiwara, S., A. Yamamoto, K. Ogawa, A. Ozaki, and Y. Koyanagi, "Attenuation characteristics of the SAR in a COST244 phantom with different EM source locations and size," *Proceeding of ISAP'04*, 793–796, Sendai, Japan, 2004.

30. Burke, G. J. and A. J. Poggio, *Numerical Electromagnetics Code (NEC): Method of Moments,* US Naval Ocean Systems Centre, Rep. No. TD116, 1981.

31. Mason, P. A., W. D. Hurt, T. J. Walters, J. A. D'Andrea, P. Gajsek, K. L. Ryan, D. A. Nelson, K. I. Smith, and J. M. Ziriax, "Effects of frequency, permittivity, and voxel size on predicted specific absorption rate values in biological tissue during electromagnetic-field exposure," *IEEE Trans. Microw. Theory Tech.*, Vol. 48, No. 11, 2050–2058, Nov. 2000.